Analysis of event stratigraphy and hydrological reconstruction of low-frequency flooding: A case study on the Fenhe River, China

Yuqin Li [a,b,c,*], Chunchang Huang [a,b], Huu Hao Ngo [c,*], Shuyan Yin [a,b], Zhibao Dong [a,b], Yuzhu Zhang [d], Yinglu Chen [e], Yujie Lu [f], Wenshan Guo [c]

[a] School of Geography and Tourism, Shaanxi Normal University, Xi'an, Shaanxi 710119, PR China
[b] National Demonstration Centre for Experimental Geography Education, Xi'an, Shaanxi 710119, PR China
[c] Faculty of Civil and Environmental Engineering, University of Technology, Sydney, NSW 2007, Australia
[d] College of Urban and Environmental Sciences, Northwest University, Xi'an 710127, PR China
[e] State Key Laboratory of Estarine and Coastal Research, East China Normal University, Shanghai 201100, PR China
[f] Faculty of Geographical Science, Beijing Normal University, Beijing 100875, PR China

* Corresponding author.
E-mail addresses: liyuqin@snnu.edu.cn (Y. Li), HuuHao.Ngo@uts.edu.au (H.H. Ngo).

Keywords:
Case study
Low-frequency flooding
Event stratigraphy
Magnitude
Frequency

A B S T R A C T

Low-frequency but high-magnitude flooding is becoming more frequent and can be well-documented by event stratigraphy. Low-frequency flooding deposits (LFDs) were discovered during a field investigation in the Holocene loess-palaeosol profile at Xucun (FHXC), which is situated at the front of the second terrace (T_2) along the middle Fenhe River. A multi-prong approach combining geochemical and sedimentological indexes (i.e. concentrations of Cr, V, Ni, Co, Cu, Zn, Rb, Mn, Pb, and Sr, magnetic susceptibility, and particle size distribution) was used to distinguish the sedimentary characteristics and environmental dynamics of LFDs. These proxies show that LFDs were well sorted clayey silt and carried in suspension during high-energy extreme flooding currents with: firstly, a high water level; and secondly, the river having a relatively stagnant environment. Based on the flooding stage indicators, magnitudes of the low-frequency flooding discharges at the site were reconstructed to be 13,480–13,590 m^3/s. The timing of the identified low-frequency flooding cluster episode was dated to 4200–3900 a BP by the Optically Stimulated Luminescence (OSL) dating technique. It agreed well with stratigraphic correlations of other existing well-dated flooding profiles in the middle reaches of the Yellow River. This case study presents long-term low-frequency flooding records and their sedimentary dynamics based on high spatial–temporal resolution systematic event stratigraphy, which advances understanding low-frequency flooding generation mechanism and improves upon predictions for occurrences and magnitudes of future extreme flooding.

1. Introduction

Low-frequency flooding is a rare event and barely observed in small basins. It is characterized by a high magnitude, and this relates to the lower quantile (<0.1%) of long-term flooding frequency distribution (Kjeldsen et al., 2014; Strupczewski et al., 2017; Wesemael et al., 2019). Global warming amplifies increases in the frequency and magnitude of low-frequency flooding. In recent decades, low-frequency flooding as the most devastating type of natural disasters in Japan (Tanaka et al., 2020), South Korea (Bae and Chang, 2019) and China (Hu et al., 2017; Zhang et al., 2017; Peng et al., 2018; Xian et al., 2018; Kundzewicz et al., 2019), is becoming frequent with an increasing magnitude. In 2013, more than 3.70 million people were affected by mega floods with a direct loss of CNY 37 million in the Amur River basin (Jia et al., 2020). It has been reported that more than 279 rivers in China flooded with higher flow stages than the warning water level in 2019. And direct flooding losses totaled CNY 106.05 billion, there were 35.26 million people were flooded, 338 flood-related deaths, and 650,000 houses were destroyed in 2018. Consequently, analyzing the low-frequency flooding characteristics including magnitude, frequency and timing is urged to predict and manage future flooding events.

Pre-instrumental data from historical documents or geological archives, e.g. lake sediments and fluvial deposits are of great significance to reconstruct low-frequency flooding over centennial-to-millennia

timescales. Furthermore, reconstructions of palaeofloods using slackwater deposits were conducted in East Asia including Japan (Grossman, 2001; Ishii, et al., 2017), South Korea (Kim, et al., 2017) and Mongolia (Kim and Tanaka, 2017). Fluvial low-frequency flooding deposits provide long-lasting evidence of peak water levels, and typically consist of silt-textured depositional layers within vertical sedimentary sequences preserved on the front terraces of the Yellow River (Huang et al., 2012; Li and Huang, 2017; Li et al., 2019). Long-term flooding datasets incorporated by low-frequency flooding events can reveal flooding cluster episodes and climate abrupt variations. A long-term flooding discharge-frequency relation can help to improve our assessment of modern flood risks and regional climate changes.

The Fenhe River, one of the major tributaries of the Yellow River, the main source of water in Shanxi province, and a key river for understanding long-term evolution of Chinese civilization, was selected as a case study (Fig. 1a). Its basin is a region where industry and population are widely distributed, and it generates 46% of the gross industrial output and is home to 41% of the entire province's population (Li et al., 2015). The per capita water resources in Shanxi province amount to 381 m^3, which is less than 20% of China nationally and it is the worst affected province in China (Sun et al., 2013). Given that increases in water consumption and overexploitation are threatening the basin's water supplies, it is imperative to document a local quantitative long-term flooding sequence so that a more accurate and reliable magnitude and frequency of flooding is recorded. This will enable water conservation projects to be designed for the purpose of flood risk assessment and reclamation in the Fenhe River basin.

According to historical records and observations, there were 150

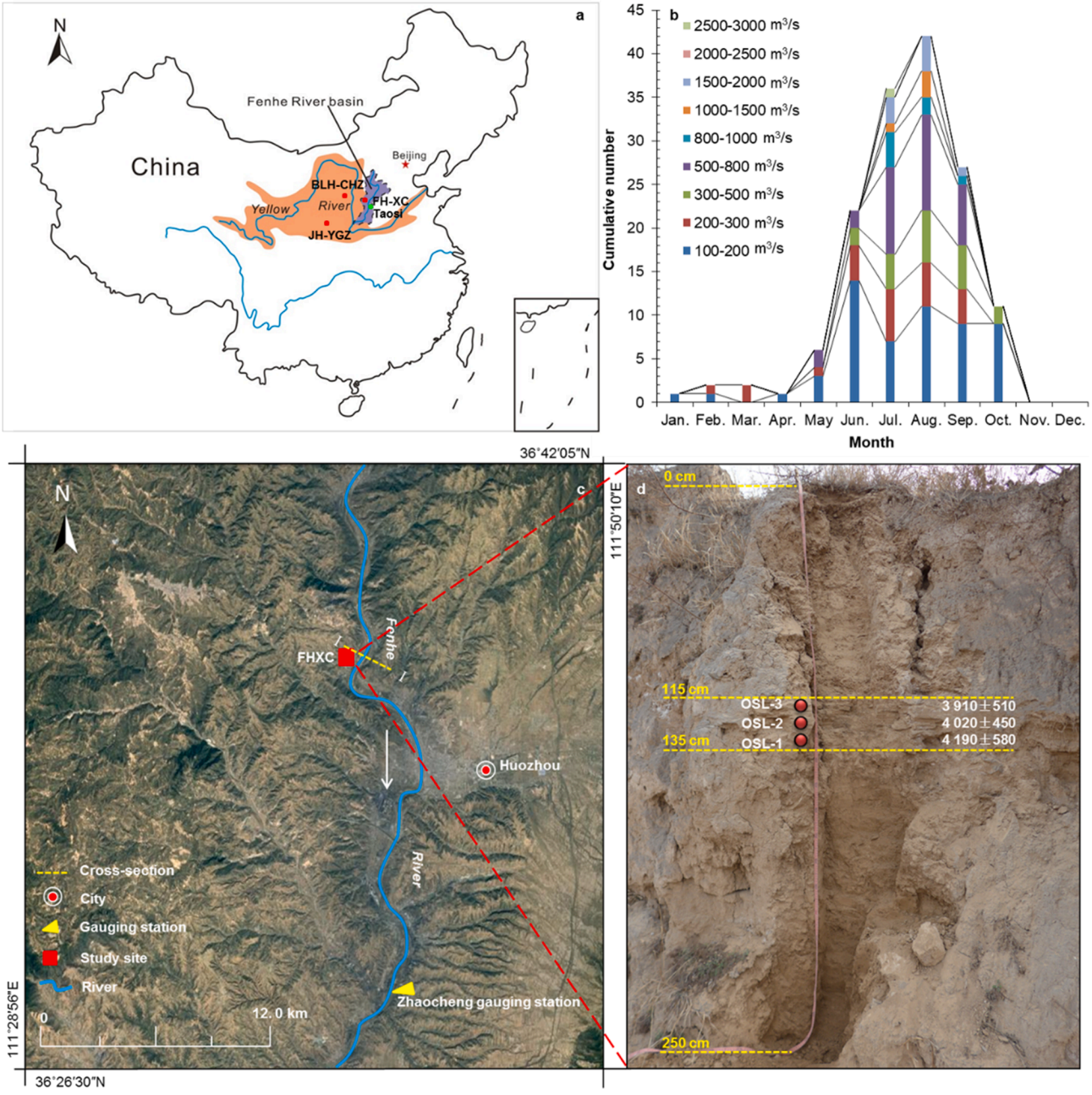

Fig. 1. (a) Location of the Fenhe River basin in central China, showing the position of river and study sites along the middle reaches of the Yellow River. (b) Statistics of different flooding magnitudes in the Fenhe River basin from 1951 to 2008. (c) Google Earth satellite image showing the location of the Xucun (FHXC) study site and gauging station on the middle reaches of the Fenhe River. (d) Photo of the sampling profile at the Xucun (FHXC) site.

major flooding events (peak discharge ≥100 m^3/s) from 1951 to 2008 in the Fenhe River basin (Fig. 1b), especially the middle and downstream sections which were flooded almost every two years. In the basin, the designed river conservation systems refer to flood discharges occurring every 20 or 100 years. However, recorded data on flooding events are too recent locally (they only began during the 1950 s) and do not reveal actual trends in flooding on millennial and centennial timescales (Baker, 1987; Benito et al., 2015). Consequently, only a few decades of observed records are available, limiting our ability to understand the characteristics of low-frequency flooding events and long-term variations (Liu et al., 2015). Till now there has been no hydrological reconstruction focused on long-term low-frequency flooding in the Fenhe River. Hence, event stratigraphies are necessary to obtain the quantitative datasets of long-term flooding events, such as water level, discharge, and velocity.

In order to further reveal long-term flooding cluster episodes and climate abrupt variations, clarify the relationship between regional hydro-climatic deterioration and prehistoric cultural decline, we have carried out extensive field investigations on event stratigraphies along the Fenhe River. In this study, we focus on (1) explain the connection between sedimentary characteristics and environmental dynamics of LFDs; (2) reconstruct the magnitude and frequency of low-frequency flooding events; and (3) understand the historical impact of low-frequency flooding events on local human settlements. Thus, this case study shedding new light on the quantitative relationship between event stratigraphy and magnitude of the low-frequency flooding on the Fenhe River and its response to climate abrupt variations.

2. Case study area

The Fenhe River, which is the second largest tributary of the Yellow River, has its source in the Guanqin Mountains at 1670 m a.s.l., and after 695 km flows into the Yellow River (Fig. 1a). It has many tributaries with a sinuosity of 1.68 and is characterized by a dendritic hydrometric network (Li et al., 2015). Located in the eastern Loess Plateau region, its basin has a drainage area of 39,471 km^2 and average gradient of 1.11‰ in the middle reaches of the Yellow River in central China (Yang et al., 2018). It has a temperate monsoonal climate, typified by large seasonal amplitudes in temperature and precipitation. The mean temperature is about 9 ℃ and average annual precipitation is about 504 mm in the basin (Sun et al., 2013; Li et al., 2015). Due to the influence of the East Asian Summer Monsoon (EASM), 84.7% of the major flooding along the Fenhe River occurs from June to September. This event is triggered by local short-duration heavy rainstorms that account for almost 80% of the total annual rainfall during the rainy season (Fig. 1b).

Zhaocheng gauging station (36°23′N, 111°40′E) was originally built in 1951 on the middle reaches of the Fenhe River to ascertain hydrological telemetry. From 1951 to 2008 a total of fifty-eight maximum annual peak discharge data was gathered from this gauging station. Two documented floods occurred at the station in 1843 and 1917 with peak discharges of 5450 m^3/s and 3740 m^3/s, respectively. As one of the birthplaces of Chinese civilization, numerous archaeological sites distributed throughout the Fenhe River basin were dated to the late Longshan Culture (4400–4000 a BP) and Xia-Shang periods (4000–3100 a BP) (Li et al., 2017a). The Taosi site (4300–3900 a BP), which is located at a higher elevation on the terrace (600 m a.s.l.) of the Fenhe River, is the largest settlement in the middle Yellow River valley; it represents the origins of Chinese civilization (Li et al., 2014).

3. Methods

3.1. Field work

Detailed post-event field investigations of low-frequency flooding marks and hydrological parameter measurements of channel cross-sections were undertaken along the course of the Fenhe River. The well-preserved profile consisting of low-frequency flooding deposits (hereafter, LFDs) and providing evidence for low-frequency flooding reconstructions came from the Xucun (FHXC) site (36°36′56″N, 111°40′05″E) located at Linghuo Canyon in the middle reaches of the Fenhe River (Fig. 1c, d). Two alluvial terraces were observed along the river valley. The first terrace (T_1) is 8–10 m and the second terrace (T_2) is 16–24 m above the Fenhe River's normal water level. The FHXC profile with a top elevation of 573 m a.s.l., situated at the front of the second terrace (T_2) on the west bank is approximately 22 m above the normal water level. Xucun village began during the Xia Dynasty (2070-1600 BCE) and – according to the archaeological discoveries – served as a ferry point for transporting passengers and goods (Li et al, 2014). In total, fifty samples were collected at 5 cm intervals in situ for sedimentary analysis. Three optically stimulated luminescence (OSL) samples of flooding event stratigraphy were obtained from the FHXC profile to determine the chronology. Moreover, the quartzite sandstone bedrock channel which represents relative stability was suitable for hydrological calculations as attempted by this study.

3.2. Sedimentological and geochemical analysis

For more details concerning characteristics, transportation processes, and sedimentary environment of the LFDs in the middle reaches of the Fenhe River, multi-proxy indexes of all fifty samples, including the geochemical distribution of elements (GDE), magnetic susceptibility (X) and particle size distribution (PSD), were measured at the Shaanxi Normal University. Geochemical analysis of trace elements were measured using a Panalytical PW2403 X-Ray fluorescence spectrometer (Guo et al., 2014). Duplicate samples, blank samples, and standard reference samples (GSS-1 and GSD-12) were all implemented to control the quality of the experimental work. Both low frequency (X_{lf}) (470 Hz) and high frequency (X_{hf}) (4700 Hz) magnetic susceptibilities were detected when using a Bartington MS2 meter. Particle size distributions (PSD) of samples were determined using a Malven Mastersizer-S laser analyzer with 100 bins ranging from 0.02 to 2000 μm, following the removal of secondary carbonates and organic matter with HCl (10%) and H_2O_2 (30%) and adding a dispersant of $(NaPO_3)_6$ (Friedman et al.,1992). The parameters were calculated statistically with Folk and Ward's (1957) method. Determining the color of stratigraphic sequences meant referring to the Munsell color chart.

3.3. OSL dating

The chronology of low-frequency flooding events was understood using the OSL dating program in the TL/OSL dating laboratory at Shaanxi Normal University. The OSL measurements of 90–125 μm grain fraction were done using a RisØ TL/OSL-DA-20 reader equipped with a $^{90}Sr/^{90}Y$ beta source delivering 0.081 Gy/s and an infrared laser diode (830 nm, ~145 mW/cm^2). The reader simulated the quartz particles with blue light (470 ± 30 nm, ~50 mW/cm^2) LEDs (Grün, 2003; Guo et al., 2018; Knight and Evans, 2018). For all samples, the uranium (U), thorium (Th), and potassium (K) content was tested by the neutron activation analysis (NAA) method at the China Institute of Atomic Energy, Beijing. The gravimetric water content was equal to the ratio of the mass of water to the mass of samples after drying in an oven. The equivalent dose (De) was determined using the single aliquot regenerative (SAR) protocol (Murray and Wintle, 2000). All of the pretreatments and measurements were conducted in the OSL/TL Dating Laboratory, Shaanxi Normal University.

3.4. Magnitude reconstructions

The core of the experimental strategy in this study consisted of reconstructing the flooding peak stage and quantizations of the peak discharge. In bedrock canyons, rivers have slackwater environments at the time of the flooding peak stages appear, and the flooding could be regarded as a stationarity flow. Peak stages of the low-frequency

flooding were estimated using the slackwater flow method (Guo et al., 2017). Each peak stage (*PS*) is summed from the bottom elevation (*BE*) of end-point LFDs and the slackwater depth (*SD*). The slackwater depth (*SD*) is calculated by the ratio of the LFD thickness (*T*) to the bulk of suspended sediment load (SSL) of the flood (*P*, %), which is the ratio of the volume of SSL in floodwater to the volume of floodwater. As a result, the *PS* was inferred from the following equations:

$$PS = BE + SD \tag{1}$$

$$SD = TP^{-1} \tag{2}$$

where *P* was inferred from the ratio of the suspended sediment concentration in floodwater at the cross-section to the specific weight of SSL (i.e. 2650 kg/m^3). The value of *P* in palaeoflood can often be insteaded by that of the SSL in the modern large flood (Guo et al., 2017). According to the maximum SSL of 770 kg/m^3 which was observed at the Zhaocheng gauging station cross-section (Fig. 1b) in the middle Fenhe River during the large flood that occurred on May 10, 1969, the parameter *P* estimation is about 29%. The peak discharge of the low-frequency flooding was simulated employing the Slope-area method (SAM), the most commonly utilized method in palaeoflood hydrology (Li and Huang, 2017). This method is based on Manning's Equation:

$$Q_p = n^{-1}(AR^{2/3}S^{1/2}) \tag{3}$$

where Q_p is the peak discharge of the flooding flow; *A* is the cross-sectional area of the flow at the flooding stage; *n* is the roughness coefficient of the stream bed; *R* is the hydraulic radius which is the ratio of the cross-sectional area (*A*) of the stream to its wetted perimeter; and *S* is the channel slope (Gordon et al., 2004). The Manning's roughness coefficient *n* was obtained from the equation as follows:

$$n = (n_l + n_m + n_r)/3 \tag{4}$$

where roughness values with suffixes of *m*, *l*, and *r* indicate the main channel and flood channel to the left and right of the river, respectively. Roughness values *n* were assigned based on the Fenhe River's channel properties and by referring to the Hydrological Calculation Norms for Hydraulic Engineering in China. The river channel geometry and slope in the middle reaches were measured at the FHXC site using an electronic distance measurer and a GPS in association with large-scale contour maps.

4. Results and discussion

4.1. Characteristics of LFDs stratigraphy

Stratigraphic sequences are well exposed and demarcations are clearly differentiated in the FHXC profile (Fig. 1d). A typical flooding sediment unit, representing a phase of frequent extreme flooding, is intercalated into the mid-Holocene palaeosol (S_0) in this profile and divides the S_0 into two parts: S_{01} and S_{02}. Specific stratigraphic classifications and systematic descriptions of the FHXC profile are presented in Table 1. Field evidence made it possible to characterize the deposits created by the low-frequency flooding event as composed of dull yellow orange, parallel or waving beddings, and moderately to well sorted strata (Table 1). Due to sedimentary features, namely Munsell color, texture and structure, the flooding unit was further subdivided into four sub-layers (LFD1-1, LFD1-2, LFD1-3, and LFD1-4). These records suggest that each sub-layer's sedimentation represents an individual flooding event and the key to how much hydrodynamic force was evident.

To carry out source identification effectively, it is necessary to analyze the distribution of trace elements in each stratigraphic sequence of the FHXC. These analyses help us to fully understand the geochemical characteristics of the Fenhe River flooding sediments and variations in regional climate. Also, the geochemical baseline values of elements in the parent materials represent the background levels of elements in the sediments of the study area. The Cr, V, Ni, Co, Cu, Zn, Rb, Mn, Pb, and Sr content in the FHXC profile were in the following respective ranges: 63.3–77.1, 79.5–101.9, 28.7–35.1, 12.3–19.2, 22.8–30.6, 63.9–78.4, 83.7–106.6, 572.4–717.8, 19.9–25.3 and 195.3–230.2 ppm. Trace elements' geochemical distributions of stratigraphic sequences further confirmed our stratigraphic subdivisions in the FHXC profile. The geochemical concentrations of the tested elements in TS, L_0 and S_{01} layers were much larger than the relevant background values of the elements in L_1, meaning that the trace metals accumulated in L_0 and S_{01} had resulted from weathering and pedogenic modification processes. Especially, S_{01} was fully matured during the warmest and wettest Holocene climatic optimum with intensive pedogenesis in favor of trace elements accumulations (Huang et al., 2012). Another interesting point is that TS in the surface was disturbed by anthropogenic activities (such as mineral exploiting and metal smelting in the Fenhe River basin since 1500). However, variations in the tested trace elements content in the LFDs layers appeared to rapidly decrease between S_{01} and S_{02}, which were formed in the mid-Holocene (Fig. 2). The mean concentrations of Cr, V, Ni, Co, Cu, Zn, Rb, Mn, Pb, and Sr in the LFDs were in the 65.1, 84.6, 29.8, 13.4, 24.1, 65.4, 93.8, 613.8, 21.0 and 211.6 ppm ranges, respectively. The amounts of ten trace elements in LFDs were all smaller than those of the parent materials L_1 (*Malan* loess) at the bottom of the FHXC profile, suggesting that the LFDs had undergone long-distance transportation by flooding flows. It also indicated that their origins were formed differently from the parent materials. A major sink for trace elements suggests that the LFDs underwent a series of physicochemical changes, such as reduction reaction, leaching, and migration in the process of flooding inundation. Remarkable peaks present at the boundary between the top of the flood deposit (LFD1-4) and bottom of the S_{01} at about 125 cm depth, suggests that LFDs were not affected by weathering and pedogenesis, but the higher location of the deposition during high flooding stage represents the more powerful uplift force of flooding in the internal hydrodynamics scenario (Li et al., 2019). Results enable a differentiation of the LFDs from loess and palaeosols, also show that some climate abnormalities existed with extreme flooding in the

Table 1
Stratigraphic subdivisions and sedimentary descriptions of the FHXC profile with flooding sediments in the middle reaches of the Fenhe River.

Depth (cm)	Stratigraphic sequence	Color	Sedimentary descriptions
0 ~ 30	Top soil (TS)	Dull brown (7.5YR6/4)	Silt, medium granular blocky structure, friable, loose porous, abundant plant roots, some bio-pores.
30 ~ 50	Recent loess (L_0)	Dull orange (7.5YR7/3)	Silt, massive blocky structure, very loose, friable, some bio-pores, few plant roots.
50 ~ 115	Palaeosol (S_{01})	Dull reddish brown (5YR5/4)	Clay, columnar blocky structure, relatively firm, moderately abundant bio-pores and some secondary calcite deposit (pseudomycelia) in the pores.
115 ~ 135	Low-frequency flooding deposits (LFDs)	Dull yellow orange (10YR7/4)	Clayey silt, massive blocky structure, very loose, some successive horizontal layers with white calcium powder inserted, individual layer thickness of 5 cm.
135 ~ 195	Palaeosol (S_{02})	Dull reddish brown (5YR5/4)	Clay, columnar blocky structure, relatively density, abundant bio-pores and some secondary calcite deposit and some earthworm burrows.
195 ~ 235	Transitional loess (L_t)	Dull orange (7.5YR6/4)	Silt, massive blocky structure, very loose, friable, some small carbonate concretions.
235~?	Malan loess (L1)	Dull yellow (10YR7/3)	Silt, massive blocky structure, very friable, some bio-pores.

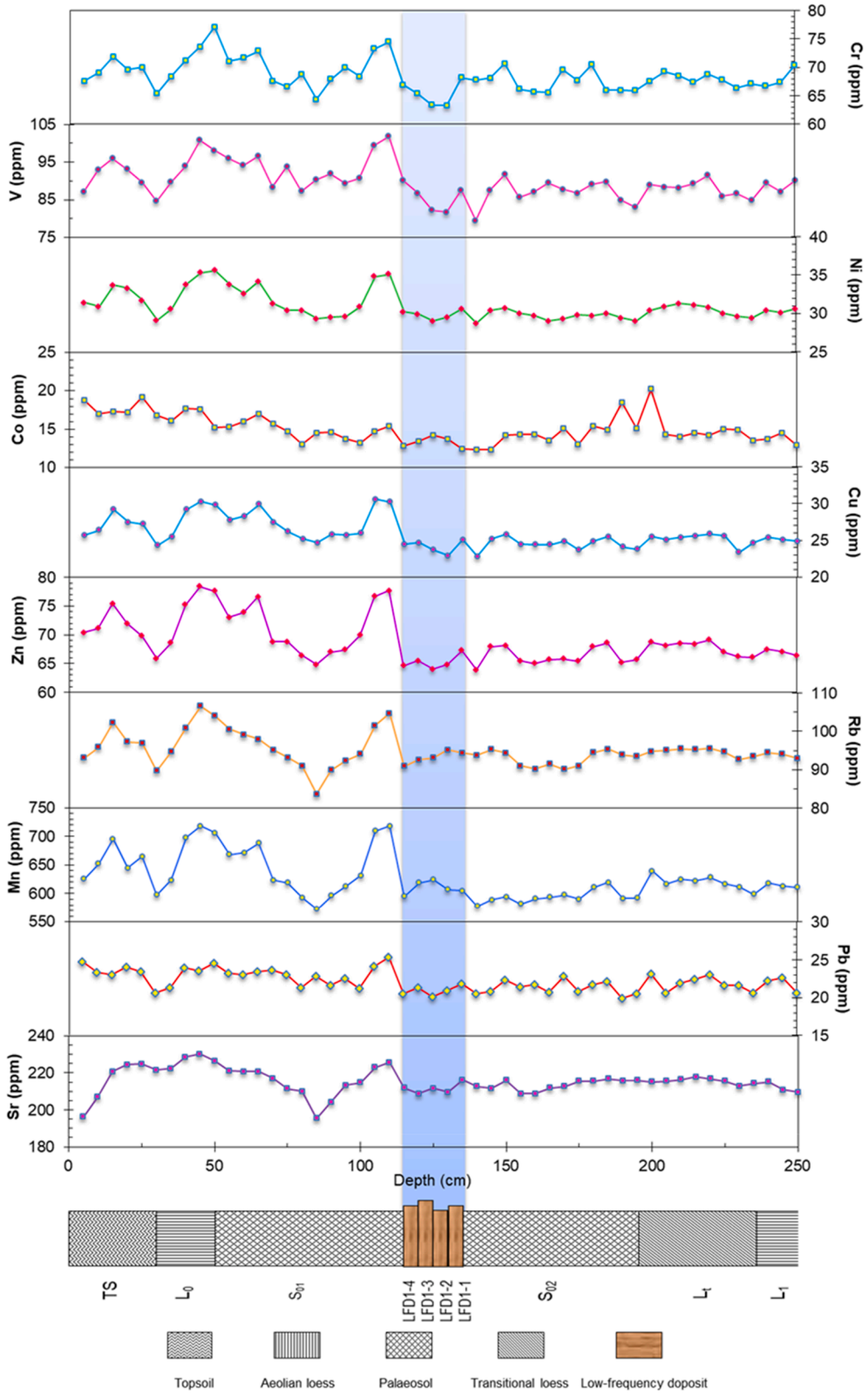

Fig. 2. Trace elements' geochemical distribution of stratigraphic sequences from the FHXC profile in the middle reaches of the Fenhe River.

mid-Holocene at the study site.

Magnetic susceptibility (X) was successfully used to identify flooding deposits from loess and palaeosol sequences in the Yellow River basin (Huang et al., 2012). As shown in Fig. 3, the trend variations of X_{lf} and X_{hf} curves in the FHXC profile are consistent. The X_{lf} values of LFD samples in the FHXC profile vary from 37.8 to 42.1 $\times 10^{-8}$ m^3/kg with an average value of 39.6 $\times 10^{-8}$ m^3/kg, and this is lower than the mean values of eolian loess (L_0 and L_1) (44.7 and 41.4 $\times 10^{-8}$ m^3/kg) and the mean values of mid-Holocene palaeosol (S_{01} and S_{02}) (43.3 and 42.8 $\times 10^{-8}$ m^3/kg). In a flooded environment, the magnetite usually presents selective dissolution, which leads to X_{lf} values of LFD samples being low. The differences in magnetic susceptibility of the FHXC profile indicate

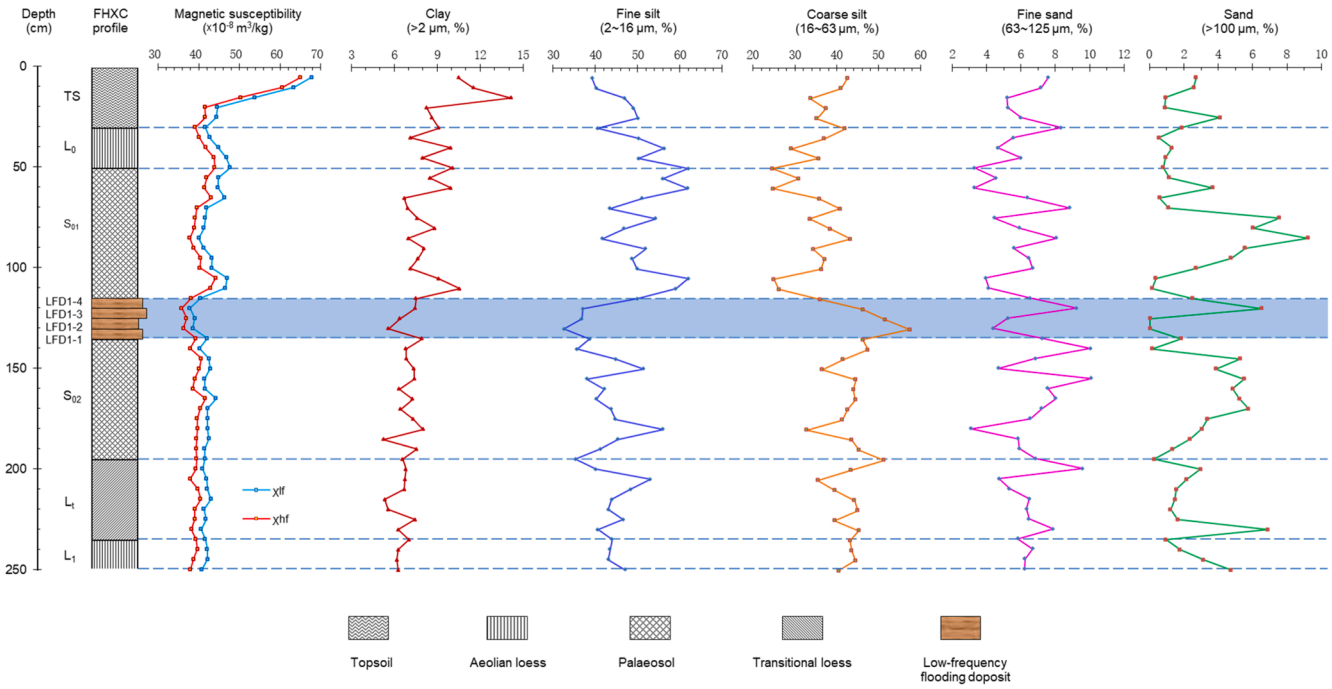

Fig. 3. Stratigraphic column, magnetic susceptibility and particle size distribution curves of the FHXC profile with LFDs in the middle reaches of the Fenhe River.

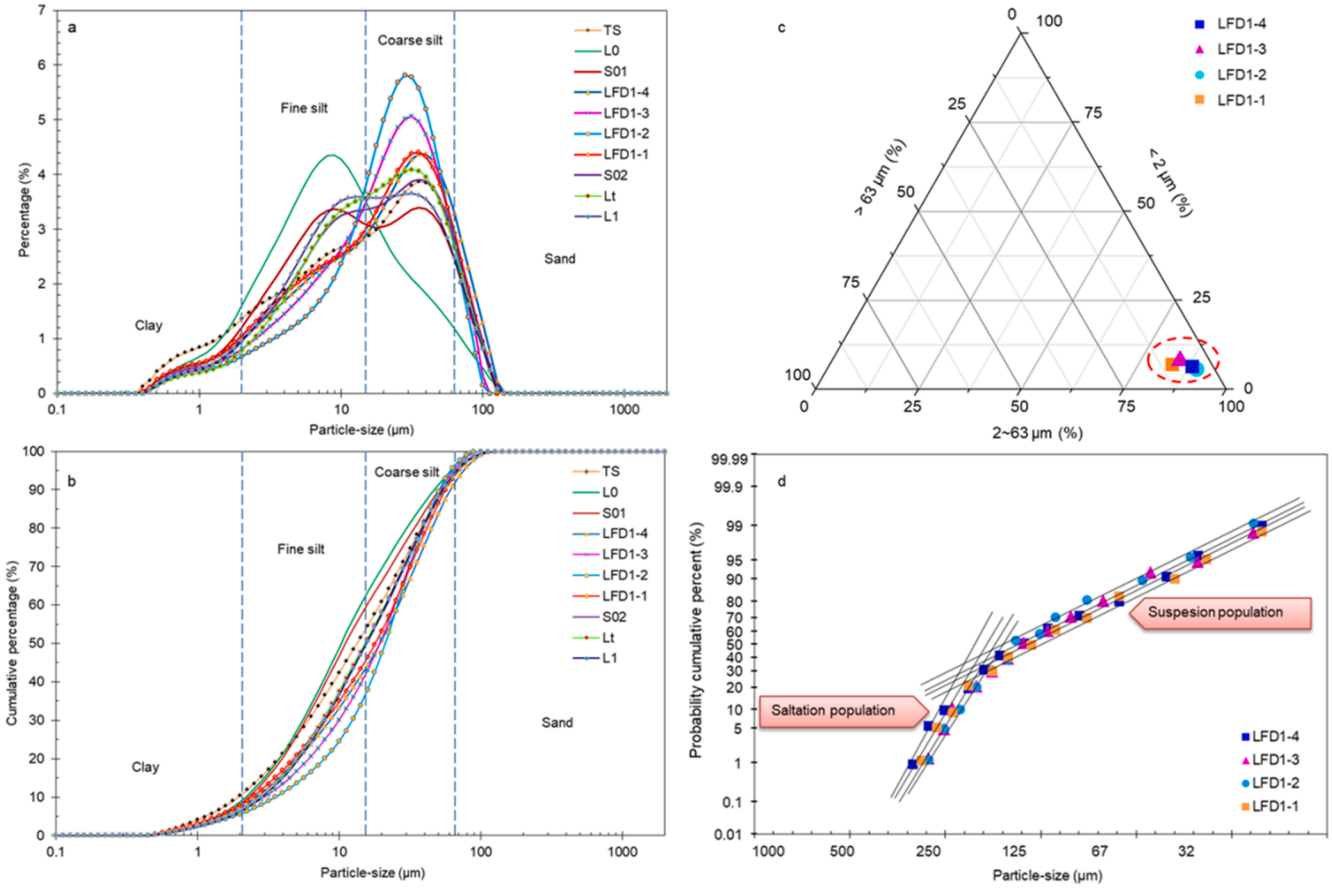

Fig. 4. (a) Particle size distribution frequency curves of samples from the FHXC profile in the middle reaches of the Fenhe River. (b) Particle size cumulative frequency curves of samples from the FHXC profile. (c) Triangular diagram of particle size compositions from the LFDs, loess and palaeosols. (d) Particle size probability cumulative curves of LFDs at the FHXC site.

that the LFDs formed during or shortly after flood peak recession without experiencing weathering and pedogenesis. Furthermore, their traits depend on the suspended sediments being carried by flooding flows.

4.2. Sedimentary environment of LFDs

Particle size analysis provides a more precise identification and characterization of the flooding sediments and their depositional setting (Huang et al., 2017). The particle size parameters reveal depositional process, hydrodynamic conditions and transportation mechanism in this stretch of the river. The PSD curves in Fig. 3 reveal that the amounts of coarse silt (16–63 μm) in the LFDs are higher than those of aeolian deposits (including TS, L_0, L_1, L_t and S_0) in the FHXC profile and the typical loess (the amount of 42.8%) in this region (Li et al., 2013); in contrast, the amount of fine silt (2–16 μm) are smaller than those of aeolian deposits in the FHXC profile and the typical loess (the amounts of 47.6%) in this region (Li et al., 2013). Thus, the LFDs are dominated by coarse silt. The amounts of fine sand (63–125 μm) and sand (>100 μm) in the LFDs are lower than those of aeolian deposits (including L_1, L_t and S_0), but they all are less than 10% in the profile. It means that the LFDs and aeolian deposits were delivered by different driving forces: one is northwest wind, the other is flood. The frequency curves of PSD in the palaeosol (S_{01} and S_{02}) and loess (L_0, L_1 and L_t) exhibit two peak values (6–12 μm and 35–55 μm), but the LFDs curves in the FHXC profile present a single peak value (25–45 μm) (Fig. 4a).

The particle size cumulative frequency curves show that aeolian deposits (loess and palaeosol) are dominated by fine silt, while the LFDs are mainly composed of coarse silt in the FHXC profile (Fig. 4b). Median particle size (*Md*) values of LFDs ranging from 17.99 μm to 21.12 μm and their mean particle size (*Mz*) values ranging from 22.62 μm to 24.63 μm are higher than those of other stratigraphic sequences in the FHXC profile. The combination of PSD frequency curves, *Md*, and *Mz* indexes means that these LFDs are dominated by coarse-grained sediments, confirming that high energy sedimentation had occurred in this LFDs unit. Furthermore, the triangular diagram of PSD demonstrates that all the LFDs layers in the FHXC profile are clayey silt in nature and different from loess and palaeosols (Fig. 4c).

The proportions of clay in the deposits reflect the link between finer composite particles in stagnant flooding with low velocities. Particle size probability cumulative curves illustrate that the LFDs were deposited mainly from suspension load fraction transported by the flooding with an average proportion of about 72%, while saltation population accounted for 27% (Fig. 4d). Sorting (σ) values between 1.48 and 1.77 mean that the LFDs are well sorted. The sharpness or peakedness of the particle size frequency curve and the degree of symmetry of particle size distribution are measured by the kurtosis (*Kg*) of 1.01 and skewness (*Sk*) of − 0.30, respectively. These particle size parameters show that LFDs are mostly coarse silt, well sorted, coarse skewed and leptokurtic. This consequently indicates that the LFDs were carried in suspension during high-energy extreme flooding currents characterized by: firstly, a high water level; and secondly, the river having a relatively stagnant environment.

4.3. Magnitudes of low-frequency flooding events

In situ reconstruction of flooding magnitudes based on geological archives can provide a real long-term record (Li et al., 2019). The bottom elevations of LFDs at the FHXC site ranged from 572.18 to 572.33 m a.s.l. Based on the slackwater flow depth method (i.e. Eqs. (1) and (2)), palaeoflood depths of four LFDs layers were between 22.35 and 22.50 m. Thus, peak stages of well-documented LFDs at the study site varied from 572.35 and 572.50 m a.s.l. (Table 2). The river channel geometry in relation to the cross-section I-I is presented in Fig. 1c and Fig. 5a, b. The river reach at the FHXC site lies in a narrow and deep bedrock valley and the channel bottom is relatively stable, resulting in a single channel system with bedrock protrusions. The bedrock-confined channel geometry at the maximum stage is known or can be approximated because no major changes can be assumed to have occurred throughout the Holocene (Liu et al., 2015; Li and Huang, 2017). Based on contour maps and field measurement, the average channel slope is 1.11‰ in this river stretch. The channel was characterized by a straight bank, some pools and shoals, clean, lower stages, more ineffective slopes and sections, stony sections, which points to the roughness coefficient *n* is 0.040 at the study site. Based on the peak stages, the maximum peak discharges of LFDs were estimated to be 13,480–13,590 m^3/s according to the SAM method (i.e. Eq. (3)) at the FHXC site (Table 2). These reconstructed palaeoflood peak discharges are larger than twice the maximum systematic gauged record of 2800 m^3/s (July 25th, 1957) at the Zhaocheng gauging station on the Fenhe River. As already found in previous studies, reconstructed palaeoflood peak discharges are higher than 2.5–3.0 times the maximum documented flooding data on the Jinghe River, Beiluohe River, and Yellow River (Huang et al., 2010; Zhang et al., 2015; Guo et al., 2017; Li et al., 2019). These reconstructed palaeoflood results agree well with the relationship between peak discharges and drainage areas of global maximum flooding events expressed by the equation $Q = 21D^{0.73}$ (Fig. 5c) and established by Baker (2006). The curves offer further convincing support to the conclusion that reconstructions of low-frequency discharges are reliable in the stable bedrock reaches of the Fenhe River.

4.4. Timing of low-frequency flooding events

A reliable chronology of each event stratigraphy was established by the OSL dating and stratigraphic correlations with other existing well-dated JH-YGZ (Huang et al., 2012) BLH-CHZ profiles (Zhang et al., 2015) in the middle reaches of the Yellow River (Fig. 1a). Stratigraphic correlations witnessed that event stratigraphies of low-frequency flooding in the FHXC profile were mainly formed in the mid-Holocene (Fig. 6). Three samples of LFDs in the FHXC profile were dated to 4190 ± 580 a, 4020 ± 450 a, and 3910 ± 580 a, respectively (Table 3). These OSL dates suggest that these low-frequency flooding events took place during 4200–3900 a BP, which is defined the beginning of the current Meghalayan age in the Holocene epoch. The interval was contemporaneous with the transition from the late Longshan Culture (4400–4000 a BP) to Xia-Shang periods (4000–3100 a BP), corresponding to the Taosi Culture period in the Fenhe River basin. Three luminescence ages of the FHXC profile also demonstrate an increase in age with depth (Table 3), reflecting the LFDs' deposition over time

Table 2
Reconstructed magnitudes of the low-frequency flooding events from the FHXC profile in the middle reaches of the Fenhe River.

Flooding events	Bottom elevation of LFD *BE* (m)	Thickness of LFD *T* (m)	Slackwater depth *SD* (m)	Palaeoflood depth (m)	Peak stage *PS* (m)	River slope S (‰)	Roughness coefficient n	Cross-section area *A* (m^2)	Wetted perimeter *L* (m)	Hydraulic radius *R* (m)	Peak discharge Q_p (m^3/s)
LFD1-4	572.33	0.05	0.17	22.50	572.50	1.11	0.04	2780.29	195.46	14.22	13,590
LFD1-3	572.28	0.05	0.17	22.45	572.45	1.11	0.04	2769.84	194.96	14.21	13,530
LFD1-2	572.23	0.05	0.17	22.40	572.40	1.11	0.04	2759.49	193.56	14.26	13,510
LFD1-1	572.18	0.05	0.17	22.35	572.35	1.11	0.04	2749.24	192.41	14.29	13,480

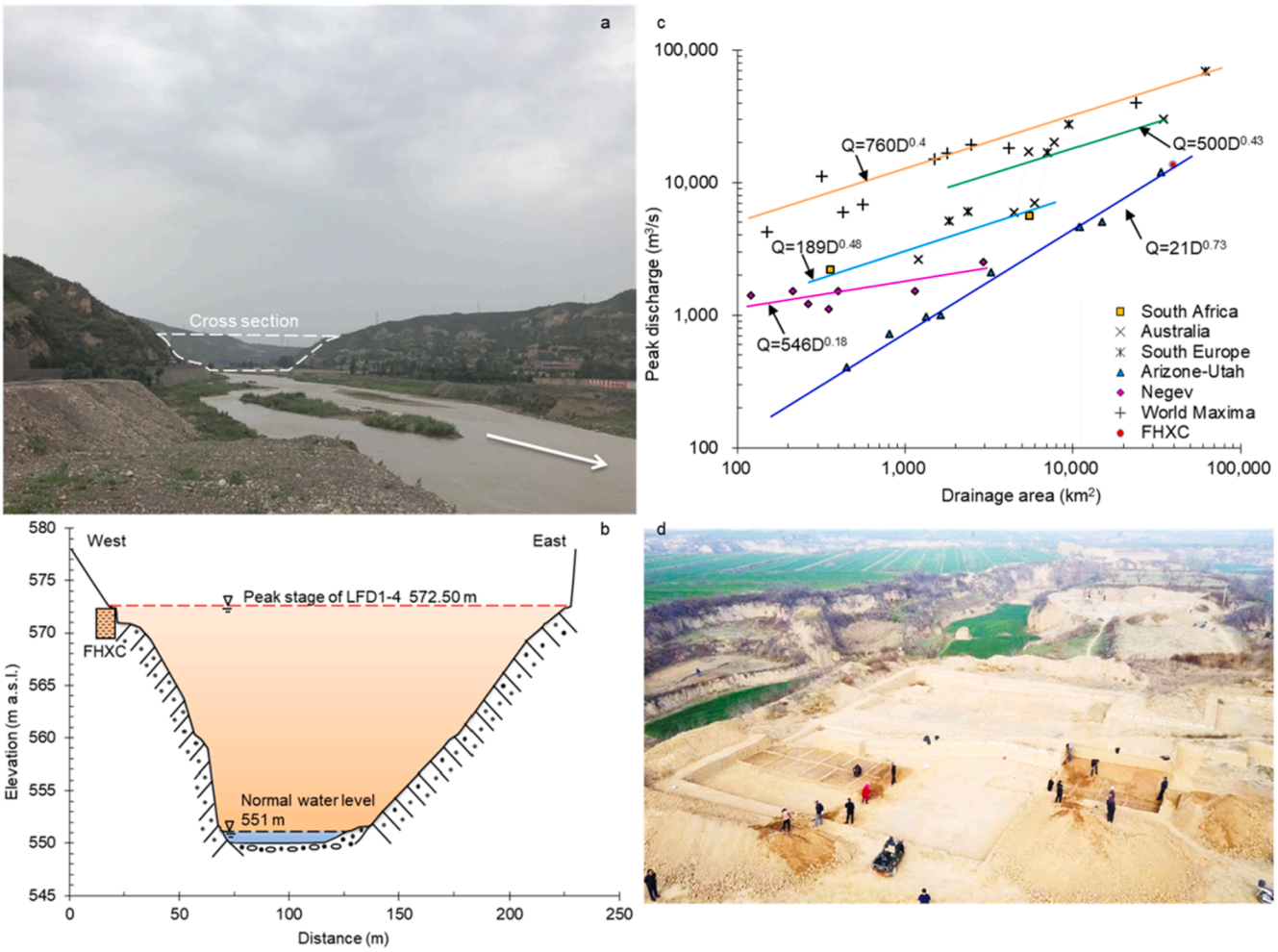

Fig. 5. (a) View of the Fenhe River channel and cross-section at the Xucun (FHXC) site, white arrow showing water flow direction. (b) Cross-section of the Fenhe River for magnitude reconstruction using the Slope-area method (SAM) at the FHXC site. (c) Reconstructed palaeoflood results in the Fenhe River fit well with the relationship between peak discharges and drainage areas of global maximum floods established by Baker (2006). (d) Photo of the Taosi site in the Fenhe River basin (http://tupian.baike.com/a4_12_11_01300000164305121429111652423_jpg.html).

under stable sedimentary environmental conditions.

Especially during the interval of climatic deterioration at 4200–3900 a BP, settlers responded to the abrupt climatic events that coincided with extreme flooding by leaving the plains that susceptible to flooding for the plateaus, hills and mountains with high elevations in the Fenhe River basin (Timmermann and Friedrich, 2016; Li et al., 2017a). In fact, the Taosi site located on the terrace with an elevation of 600 m a.s.l. was ca. 40 m higher than the water level of the Fenhe River that was further confirmed the overbank flooding occurred frequently during the period (Fig. 5d). Furthermore, episodes of social destabilization, wars, and dynastic cycles in China were more frequent during the interval (Hosner et al., 2016; Wang et al., 2016). Some other prominent low-frequency flooding records at 3900–4200 a BP of the climatic transitional period were found on the Yellow River and its other tributaries (Fig. 6), such as the Jinghe River (Huang et al., 2012) and Beiluohe River (Zhang et al., 2015). Also, it was reported that two extreme flooding events occurred at 4900–4600 a BP and 4100–3800 a BP in the middle Yangtze River that have accelerated the decline of the Shijiahe Culture (4100–3800 a BP) (Wu et al., 2017). As well, the cooling-arid climatic event at 4200 a BP was well-documented by a stalagmite from Dongge Cave (Wang et al., 2005). The late Neolithic cultures, such as the Qijia Culture in the upper Yellow River and the Laohushan Culture in southern Inner Mongolia in China terminated abruptly at 4000 a BP (Dong et al., 2013; Wang et al., 2016). In these cases, the remarkable climatic shift involving a sharp increase in occurrences of drought, cooling-arid conditions or high-magnitude low-frequency flooding played an important role in the transition of Neolithic-Bronze cultures throughout China. Consequently, the ancient settlement migrations and devastation of the Taosi Culture in the Fenhe River basin mainly resulted from the regional dramatic climate fluctuations, a finding that is consistent with frequent extreme flooding events (Li et al., 2014; Li et al., 2017a). In addition, pollen percentages from Dali Lake (Wen et al., 2017) and Gonghai Lake (Chen et al., 2015), and the stalagmite oxygen isotope values from tHeshang Cave (Wang et al., 2018), all of which are located in the domain of the East Asian summer monsoon, suggested that the monsoon precipitation fluctuated but with an overall decreasing trend in northern and central China during the period of 4200–3900 a BP, corresponding to the "4200 a BP cooling climatic event" worldwide, caused by the weaker East Asia summer monsoon (Li et al., 2015), as well as relatively strong El Niño/Southern Oscillation (ENSO) activities (Zhu et al., 2017; Sun et al., 2019; Zhang et al., 2021). Again, it indicated that extreme floods triggered by heavy rainstorms occurred in the study region, accompanied by frequent droughts during the "4200 a BP event".

4.5. *Frequency of long-term flooding events*

The log-Pearson type III (LP-III) distribution method is extensively used for flooding frequency estimation of non-continuous data series including extreme values (Schendel and Thongwichian, 2017; Solari, et al., 2017; Burn and Whitfield, 2018). A statistical analysis of

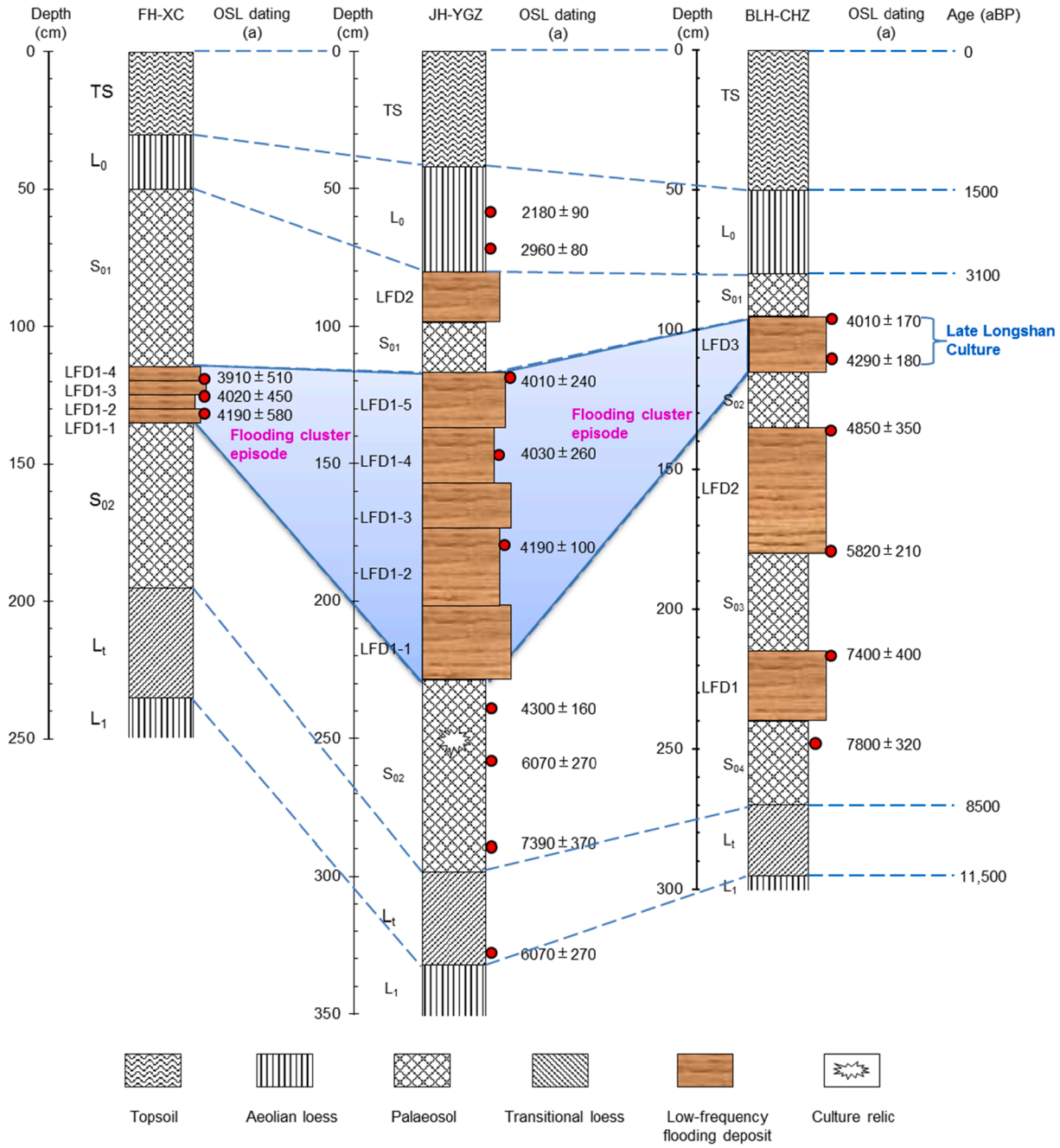

Fig. 6. Stratigraphic correlations of profile and the Holocene low-frequency flooding profiles at the FHXC site and other sites, i.e. Yangguanzhai (JH-YGZ) site (Huang et al., 2012), Caihezhan (BLH-CHZ) site (Zhang et al., 2015) with OSL dates in the middle reaches of the Yellow River.

Table 3
The equivalent dose values, dose rates and OSL ages for flooding samples from the FHXC in the middle reaches of the Fenhe River.

Sample ID	Depth (cm)	U (ppm)	Th (ppm)	K (%)	Water content (%)	Equivalent dose De (Gy)	Dose rate Gy (ka)	Age (a)
OSL-3	115–120	2.18 ± 0.3	13.11 ± 0.6	1.75 ± 0.04	19.0 ± 5	11.44 ± 1.31	2.92 ± 0.18	3910 ± 510
OSL-2	120–125	2.68 ± 0.4	14.51 ± 0.7	1.89 ± 0.04	18.5 ± 5	13.08 ± 1.21	3.25 ± 0.20	4020 ± 450
OSL-1	130–135	2.49 ± 0.4	13.95 ± 0.7	1.73 ± 0.04	17.0 ± 5	12.93 ± 1.58	3.08 ± 0.19	4190 ± 580

reconstructed low-frequency flooding, historical flooding, and observed annual flooding series (AFS) (1951–2008) at the Zhaocheng station was performed by fitting a LP-III distribution (Fig. 7). A regional long-term flooding frequency curve built as a red line in Fig. 7 reveals that frequencies of reconstructed palaeoflood peak discharges were 0.01% in the lower quantile of the curve. As a result, the reconstructed peak discharge of 13,590 m^3/s corresponds to a large return period lasting 10,000 years (Table 4). The discharges for 1000- and 100-year flooding events were 10,600 m^3/s and 4550 m^3/s, respectively. Statistics show that 78.6% of extreme floods were caused by large-scale rainstorms in

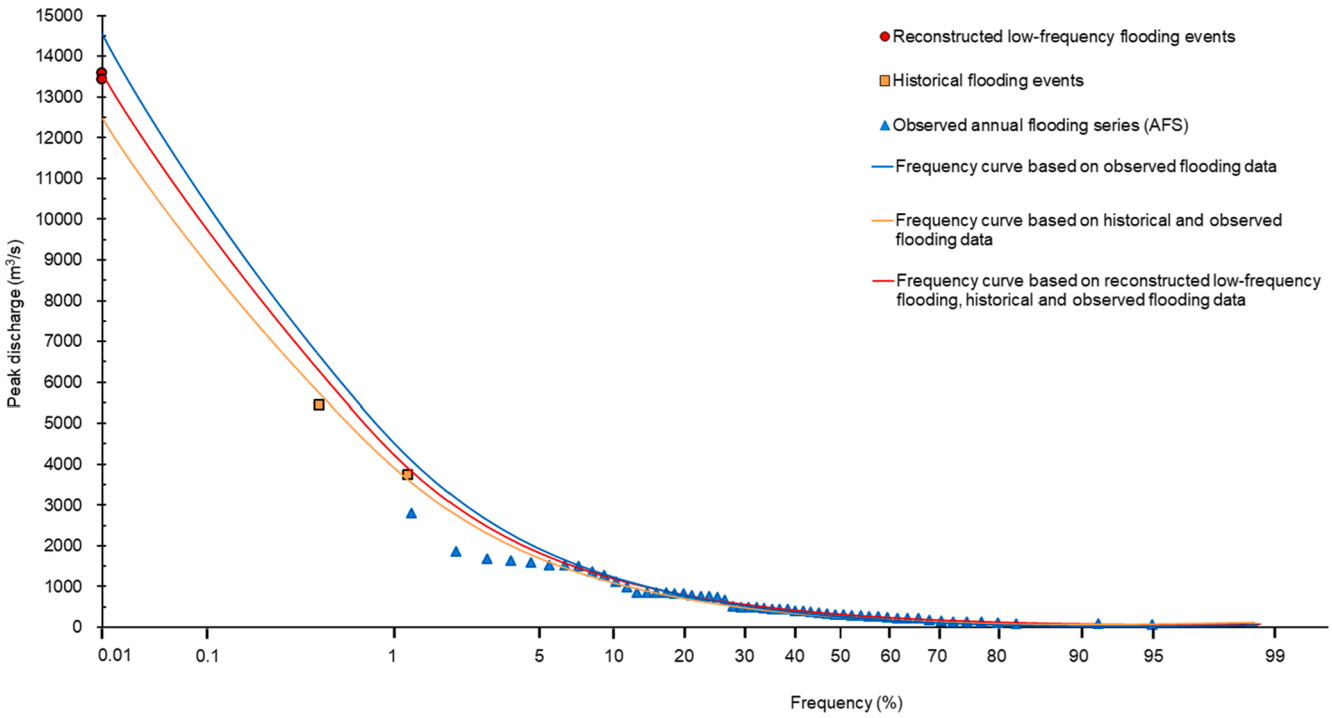

Fig. 7. Relationship between flooding frequency-magnitude and a long-term frequency curve was established by incorporating observed annual flooding series (1951 ~ 2008), historical flooding events (1843 and 1917), and reconstructed low-frequency flooding events at the Zhaocheng gauging station in the Fenhe River basin.

Table 4
The relationship between flooding peak discharges and return periods at the Zhaocheng gauging station in the Fenhe River basin.

Frequency (%)	0.01	0.1	0.2	0.5	1	2	5	10	20	50
Return period (yr)	10,000	1000	500	200	100	50	20	10	5	2
Peak discharge Q_p (m^3/s)	13,590	10,600	7520	5950	4550	3690	2600	1820	1110	371

the basin, and the flood hydrograph was characterized by a rapid rise and mitigatory recession (Shanxi Province Department of Water Resources, 2014), such as a severe flood of the Wuding River occurred in 2017 and its peak stage rose nearly 20 m in Suide County (Yao et al., 2018).

5. Conclusions

In the case study, low-frequency flooding events that occurred on the middle Fenhe River during 4200–3900 a BP were identified based on event stratigraphy. Multi-proxy indexed were applied to reveal that LFDs were well-sorted clayey silt in nature and carried in suspension during high-energy extreme flooding currents with a high water level and the river having a relatively stagnant environment. Combining the slackwater flow depths inferred by the thicknesses of LFDs, magnitudes of low-frequency flooding at the studied site were reconstructed to be 13,480–13,590 m^3/s with peak stages varying from 572.35 and 572.50 m a.s.l. at the study site. The results were larger than twice of the maximum systematic gauged record of 2800 m^3/s. And the peak discharges-drainage area relationship for the Fenhe River basin could be expressed as $Q = 21D^{0.73}$. Coupling with real low-frequency flooding data, a regional long-term magnitude-frequency curve was obtained, which improved the precise of flood risk assessment and prediction future low-frequency flooding events in the basin.

The high-magnitude low-frequency flooding events were highly sensitive to regional monsoonal climatic variability in the Holocene. A flooding clusters episode at 4200–3900 a BP is comparable with the ancient settlement migrations and devastation of the Taosi Culture in the Fenhe River basin. Moreover, synchronous high-magnitude low-frequency flooding on the Yellow River and Yangtze River played an important role in the transition of Neolithic-Bronze Age in China. These findings potentially contribute to a better understanding of the relationship between prehistoric cultural decline and regional hydroclimatic deterioration.

CRediT authorship contribution statement

Yuqin Li: Conceptualization, Methodology, Investigation, Writing - original draft, Funding acquisition. **Chunchang Huang:** Methodology, Project administration, Funding acquisition. **Huu Hao Ngo:** Conceptualization, Visualization, Writing - review & editing. **Shuyan Yin:** Investigation, Resources. **Zhibao Dong:** Supervision. **Yuzhu Zhang:** Software, Validation. **Yinglu Chen:** Software, Validation. **Yujie Lu:** Investigation, Validation. **Wenshan Guo:** Writing - review & editing.

Declaration of Competing Interest

The authors declare that they have no known competing financial interests or personal relationships that could have appeared to influence the work reported in this paper.

Acknowledgements

This research was supported by the grants from the National Natural Science Foundation of China (No. 41601020, 41971116, 41801060) and the China Postdoctoral Science Foundation (No. 2017M623113).

References

Bae, S., Chang, H., 2019. Urbanization and floods in the Seoul Metropolitan area of South Korea: What old maps tell us. Int. J. Disaster Risk Reduc. 37, 1–11. https://doi.org/10.1016/j.ijdrr.2019.101186.

Baker, V.R., 1987. Paleoflood hydrology and extraordinary flood events. J. Hydrol. 96, 79–99. https://doi.org/10.1016/0022-1694(87)90145-4.

Baker, V.R., 2006. Palaeoflood hydrology in a global context. Catena 66, 161–168. https://doi.org/10.1016/j.catena.2005.11.016.

Benito, G., Macklin, M.G., Zielhofer, C., Jones, A.F., Machado, M.J., 2015. Holocene flooding and climate change in the Mediterranean. Catena 130, 13–33. https://doi.org/10.1016/j.catena.2014.11.014.

Burn, D.H., Whitfield, P.H., 2018. Changes in flood events inferred from centennial length streamflow data records. Adv. Water Resour. 121, 333–349. https://doi.org/10.1016/j.advwatres.2018.08.017.

Chen, F.H., Xu, Q.H., Chen, J.H., John, H., Birks, B., Liu, J.B., Zhang, S.R., Jin, L.Y., An, C.B., Telford, R.J., Cao, X.Y., Wang, Z.L., Zhang, X.J., Selvaraj, K., Lu, H.Y., Li, Y. C., Zheng, Z., Wang, H.P., Zhou, A.F., Dong, G.H., Zhang, J.W., Huang, X.Z., Bloemendal, J., Rao, Z.G., 2015. East Asian summer monsoon precipitation variability since the last deglaciation. Sci. Rep. 5, 11186.

Dong, G., Jia, X., Elston, R., Chen, F., Li, S., Wang, L., Cai, L., An, C., 2013. Spatial and temporal variety of prehistoric human settlement and its influencing factors in the upper Yellow River valley, Qinghai Province, China. J. Archaeol. Sci. 40 (5), 2538–2546. https://doi.org/10.1016/j.jas.2012.10.002.

Folk, R.L., Ward, W., 1957. Brazos River bar: a study in the significance of grain size parameters. J. Sediment. Petrol. 27, 3–26. https://doi.org/10.1306/74D70646-2B21-11D7-8648000102C1865D.

Friedman, G.M., Sanders, J.E., Kopaska-Merkel, D.C., 1992. Principals of Sedimentary Deposits. Macmillan, New York, pp. 36–42.

Gordon, A.L., Zambianchi, E., Orsi, A., Visbeck, M., Giulivi, C.F., Whitworth, T., Spezie, G., 2004. Energetic plumes over the western Ross Sea continental slope. Geophys. Res. Lett. 31, L21302. https://doi.org/10.1029/2004GL020785.

Grossman, M.J., 2001. Large floods and climatic change during the Holocene on the Ara River, Central Japan. Geomorphology 39, 21–37. https://doi.org/10.1016/S0169-555X(01)00049-6.

Grün, R., 2003. Age. Exe Computer Program for the Calculation of Luminescence Dates. Unpublished Computer Program RSES, Canberra, Australia.

Guo, Y.Q., Huang, C.C., Pang, J.L., Zha, X.C., Li, X.P., Zhang, Y.Z., 2014. Concentration of heavy metals in the modern flood slackwater deposits along the upper Hanjiang River valley, China. Catena 116, 123–131. https://doi.org/10.1016/j.catena.2013.12.019.

Guo, Y.Q., Huang, C.C., Pang, J.L., Zhou, Y.L., Zha, X.C., Mao, P.N., 2017. Reconstruction palaeoflood hydrology using slackwater flow depth method in the Yanhe River valley, middle Yellow River basin, China. J. Hydrol. 544, 156–171. https://doi.org/10.1016/j.jhydrol.2016.11.017.

Guo, Y.Q., Huang, C.C., Zhou, Y.L., Pang, J.L., Zha, X.C., Fan, L.J., Mao, P.N., 2018. Sedimentary record and luminescence chronology of palaeoflood events along the Gold Gorge of the upper Hanjiang River, middle Yangtze River. J. Asian Earth Sci. 156, 96–110. https://doi.org/10.1016/j.jseaes.2017.12.034.

Hosner, D., Wagner, M., Tarasov, P.E., Chen, X., Leipe, C., 2016. Spatiotemporal distribution patterns of archaeological sites in China during the Neolithic and Bronze Age: An overview. Holocene 26 (10), 1576–1593. https://doi.org/10.1177/0959683616641743.

Hu, M.C., Sayama, T., Zhang, X.Q., Tanaka, K., Takara, K., Yang, H., 2017. Evaluation of low impact development approach for mitigating flood inundation at a watershed scale in China. J. Environ. Manage. 193, 430–438. https://doi.org/10.1016/j.jenvman.2017.02.020.

Huang, C.C., Pang, J., Zha, X., Zhou, Y., Su, H., Li, Y., 2010. Extraordinary floods of 4 100–4 000 a BP recorded at the Late Neolithic Ruins in the Jinghe River Gorges, middle reach of the Yellow River, China. Palaeogeogr. Palaeoclimatol. Palaeoecol. 289 (1-4), 1–9. https://doi.org/10.1016/j.palaeo.2010.02.003.

Huang, C.C., Pang, J., Zha, X., Zhou, Y., Su, H., Zhang, Y., Wang, H., Gu, H., 2012. Holocene palaeoflood events recorded by slackwater deposits along the lower Jinghe River valley, middle Yellow River basin, China. J. Quat. Sci. 27 (5), 485–493. https://doi.org/10.1002/jqs.2536.

Huang, C.C., Zhou, Y., Zhang, Y., Guo, Y., Pang, J., Zhou, Q., Liu, T., Zha, X., 2017. Comment on "Outburst flood at 1920 BCE supports historicity of China's Great Flood and the Xia dynasty". Science 355 (6332), 1382. https://doi.org/10.1126/science:aak9657.

Ishii, Y., Hori, K., Momohara, A., 2017. Middle to late Holocene flood activity estimated from loss on ignition of peat in the Ishikari lowland, northern Japan. Glob. Planet. Change 153, 1–15. https://doi.org/10.1016/j.gloplacha.2017.04.004.

Jia, M.M., Mao, D.H., Wang, Z.M., Ren, C.Y., Zhu, Q.D., Li, X.C., Zhang, Y.Z., 2020. Tracking long-term floodplain wetland changes: A case study in the China side of the Amur River Basin. Int. J. Appl. Earth Obs. Geoinf. 92, 1–12. https://doi.org/10.1016/j.jag.2020.102185.

Kim, S.H., Tanaka, Y., 2017. Palaeoflood records of the last three centuries from the Pyeongchang and Dong rivers, South Korea. Geomorphology 290, 211–221. https://doi.org/10.1016/j.geomorph.2017.04.028.

Kim, S.H., Tanaka, Y., Kashima, K., 2017. The history of palaeoflood and palaeoclimate recorded in the flood deposits of the Kherlen River, Mongolia. Quat. Int. 440, 118–128. https://doi.org/10.1016/j.quaint.2017.05.026.

Kjeldsen, T.R., Macdonald, N., Lang, M., Mediero, L., Albuquerque, T., Bogdanowicz, E., Brazdil, R., Castellarin, A., David, V., Fleig, A., Gul, G.O., Kriauciuniene, J., Kohnovam, S., Merz, B., Nicholson, O., Roald, L.A., Salinas, J.L., Sarauskiene, D., Šraj, M., Strupczewski, W., Szolgaym, J., Toumazis, A., Vanneuville, W., Veijalainen, N., Wilson, D., 2014. Documentary evidence of past floods in Europe and their utility in flood frequency estimation. J. Hydrol. 517, 963–973. https://doi.org/10.1016/j.jhydrol.2014.06.038.

Knight, J., Evans, M., 2018. Luminescence dating, sediment analysis, and flood dynamics on the Sabie River, South Africa. Geomorphology 319, 1–14. https://doi.org/10.1016/j.geomorph.2018.07.011.

Kundzewicz, Z.W., Su, B.D., Wang, Y.J., Xia, J., Huang, J.L., Jiang, T., 2019. Flood risk and its reduction in China. Adv. Water Resour. 130, 37–45. https://doi.org/10.1016/j.advwatres.2019.05.020.

Li, J.C., Han, L.Y., Zhang, G.M., Su, Z.Z., Zhao, Y.F., 2017. Temporal-spatial variations of human settlements in relation to environment change during the Longshan culture and Xia-Shang periods in Shanxi Province, China. Quat. Int. 436, 129–137. https://doi.org/10.1016/j.quaint.2016.11.048.

Li, Q., Liu, Y., Takeshi, N., Song, H.M., Danny, M.C., Yang, Y.K., Qi, J., 2015. The 225-year precipitation variability inferred from tree-ring records in Shanxi Province, the North China, and its teleconnection with Indian summer monsoon. Glob. Planet. Change 132, 11–19. https://doi.org/10.1016/j.gloplacha.2015.06.005.

Li, T.Y., Mo, D.W., Hu, K., Zhang, Y.F., Wang, J.J., 2013. The environmental and cultural background of the Taosi site, Xiangfen County, Shanxi Province. Sci. Geograph. Sinica 33 (4), 443–449 (in Chinese).

Li, T.Y., Mo, D.W., Kidder, T., Zhang, Y.F., Wang, H.B., Wu, Y.Q., 2014. Holocene environmental change and its influence on the prehistoric culture evolution and the formation of the Taosi site in Linfen basin, Shanxi province, China. Quat. Int. 349, 402–408. https://doi.org/10.1016/j.quaint.2014.07.054.

Li, X.G., Huang, C.C., 2017. Holocene palaeoflood events recorded by slackwater deposits along middle Yellow River, China. Quat. Int. 453, 85–95. https://doi.org/10.1111/bor.12095.

Li, Y.Q., Huang, C.C., Ngo, H.H., Pang, J.L., Zha, X.C., Liu, T., Guo, W.S., 2019. In situ reconstruction of long-term extreme flooding magnitudes and frequencies based on geological archives. Sci. Total Environ. 670, 8–17. https://doi.org/10.1016/j.scitotenv.2019.03.066.

Liu, T., Huang, C.C., Pang, J., Zha, X., Zhou, Y., Zhang, Y., Ji, L., 2015. Late Pleistocene and Holocene palaeoflood events recorded by slackwater deposits in the upper Hanjiang River valley, China. J. Hydrol. 529, 499–510. https://doi.org/10.1016/j.jhydrol.2014.11.075.

Murray, A.S., Wintle, A.G., 2000. Luminescence dating of quartz using an improved single–aliquot regenerative–dose protocol. Radiat. Meas. 32 (1), 57–73. https://doi.org/10.1016/S1350-4487(99)00253-X.

Peng, Y., Long, S.F., Ma, J.W., Song, J.Y., Liu, Z.W., 2018. Temporal-spatial variability in correlations of drought and flood during recent 500 years in Inner Mongolia, China. Sci. Total Environ. 15, 484–491. https://doi.org/10.1016/j.scitotenv.2018.03.200.

Schendel, T., Thongwichian, R., 2017. Considering historical flood events in flood frequency analysis: Is it worth the effort? Adv. Water Resour. 105, 144–153. https://doi.org/10.1016/j.advwatres.2017.05.002.

Shanxi Province Department of Water Resources, 2014. Study on floods in Shanxi Province. Zhengzhou: Yellow River Conservancy Press. pp. 121–161.

Solari, S., Egüen, M., Polo, M.J., Losada, M.A., 2017. Peaks Over Threshold (POT): a methodology for automatic threshold estimation using goodness of fit p-value. Water Resour. Res. 53, 2833–2849. https://doi.org/10.1002/2016WR019426.

Strupczewski, W.G., Kochanek, K., Bogdanowicz, E., 2017. Historical floods in flood frequency analysis: Is this game worth the candle? J. Hydrol. 554, 800–816. https://doi.org/10.1016/j.jhydrol.2017.09.034.

Sun, J.Y., Liu, Y., Wang, Y.C., Bao, G., Sun, B., 2013. Tree-ring based runoff reconstruction of the upper Fenhe River basin, North China, since 1799 AD. Quat. Int. 283, 117–124. https://doi.org/10.1016/j.quaint.2012.03.044.

Sun, Q., Liu, Y., Wünnemann, B., Peng, Y., Jiang, X., Deng, L., Chen, J., Li, M., Chen, Z., 2019. Climate as a factor for Neolithic cultural collapses approximately 4000 years BP in China. Earth Sci. Rev. 197, 1–21. https://doi.org/10.1016/j.earscirev.2019.102915.

Tanaka, T., Kiyohara, K., Tachikawa, Y., 2020. Comparison of fluvial and pluvial flood risk curves in urban cities derived from a large ensemble climate simulation dataset: A case study in Nagoya, Japan. J. Hydrol. 584, 1–816. https://doi.org/10.1016/j.jhydrol.2020.124706.

Timmermann, A., Friedrich, T., 2016. Late Pleistocene climate drivers of early human migration. Nature 538, 92–95. https://doi.org/10.1038/nature19365.

Wang, C.F., Bendle, J.A., Zhang, H.B., Yang, Y., Liu, D., Huang, J.H., Cui, J.W., Xie, S.C., 2018. Holocene temperature and hydrological changes reconstructed by bacterial 3-hydroxy fatty acids in a stalagmite from central China. Quat. Sci. Rev. 192, 97–105. https://doi.org/10.1016/j.quascirev.2018.05.030.

Wang, J.J., Sun, L.G., Chen, L.Q., Xu, L.B., Wang, Y.H., Wang, X.M., 2016. The abrupt climate change near 4,400 yr BP on the cultural transition in Yuchisi, China and its global linkage. Sci. Rep. 6, 27723. https://doi.org/10.1038/srep27723.

Wang, Y.J., Cheng, H., Edwards, R.L., He, Y.Q., Kong, X.G., An, Z.S., Wu, J.Y., Kelly, M. J., Dykoski, C.A., Li, X.D., 2005. The Holocene Asian monsoon: links to solar changes and North Atlantic climate. Science. 308, 854–857. https://doi.org/10.1126/science.1106296.

Wen, R., Xiao, J., Fan, J., Zhang, S., Yamagata, H., 2017. Pollen evidence for a mid-Holocene East Asian summer monsoon maximum in northern China. Quat. Sci. Rev. 176, 29–35. https://doi.org/10.1016/j.quascirev.2017.10.008.

Wesemael, A.V., Landuyt, L., Lievens, H., Verhoes, N.E.C., 2019. Improving flood inundation forecasts through the assimilation of in situ floodplain water level measurements based on alternative observation network configurations. Adv. Water Resour. 130, 229–243. https://doi.org/10.1016/j.advwatres.2019.05.025.

Wu, L., Zhu, C., Ma, C., Li, F., Meng, H., Liu, H., Li, L., Wang, X., Sun, W., Song, Y., 2017. Mid-Holocene palaeoflood events recorded at the Zhongqiao Neolithic cultural site

in the Jianghan Plain, middle Yangtze River Valley, China. Quat. Sci. Rev. 173, 145–160. https://doi.org/10.1016/j.quascirev.2017.08.018.
Xian, S.Y., Yin, J., Lin, N., Oppenheimer, M., 2018. Influence of risk factors and past events on flood resilience in coastal megacities: Comparative analysis of NYC and Shanghai. Sci. Total Environ. 610–611, 1251–1261. https://doi.org/10.1016/j.scitotenv.2017.07.229.
Yang, Y.G., Meng, Z.L., Jiao, W.T., 2018. Hydrological and pollution processes in mining area of Fenhe River Basin in China. Environ. Pollut. 234, 743–750. https://doi.org/10.1016/j.envpol.2017.12.018.
Yao, W.Y., Hou, S.Z., Guo, Y., 2018. Causes analysis of a flood disaster on "2017.7.26" rainstorm in Suide and Zhizhou of Northern Shaanxi. China Flood Drought Manage. 28 (9), 27–32 (in Chinese).
Zhang, Q., Gu, X.H., Vijay, P.S., Shi, P.J., Luo, M., 2017. Timing of floods in southeastern China: Seasonal properties and potential causes. J. Hydrol. 552, 732–744. https://doi.org/10.1016/j.jhydrol.2017.07.039.
Zhang, Y., Huang, C.C., Pang, J., Zha, X., Zhou, Y., Wang, X., 2015. Holocene palaeoflood events recorded by slackwater deposits along the middle Beiluohe River valley, middle Yellow River basin, China. Boreas 44 (1), 127–138. https://doi.org/10.1111/bor.12095.
Zhang, Z.P., Liu, J.B., Chen, J., Chen, S.Q., Shen, Z.W., Chen, J., Liu, X.K., Wu, D., Sheng, Y.W., Chen, F.H., 2021. Holocene climatic optimum in the East Asian monsoon region of China defined by climatic stability. Earth Sci. Rev. 212, 1–13. https://doi.org/10.1016/j.earscirev.2020.103450.
Zhu, Z., Feinberg, J.M., Xie, S., Bourne, M.D., Huang, C., Hu, C., Cheng, H., 2017. Holocene ENSO-related cyclic storms recorded by magnetic minerals in speleothems of Central China. Proc. Natl. Acad. Sci. 114 (5), 852–857. https://doi.org/10.1073/pnas.1610930114.